Chinese Chemical Letters 32 (2021) 1144–1148

Contents lists available at ScienceDirect

Chinese Chemical Letters

journal homepage: www.elsevier.com/locate/cclet

Communication

A novel synthesis of Nb_2O_5@rGO nanocomposite as anode material for superior sodium storage

Yu Zhang[a], Li Fang[a], Wang Sun[a,*], Bin Shi[b], Xiaotao Chen[b], Yujie Gu[c], Kunpeng Ding[c], Zhenhua Wang[a], Kening Sun[a]

[a] Beijing Key Laboratory for Chemical Power Source and Green Catalysis, School of Chemistry and Chemical Engineering, BIT-QUB Joint Center on Novel Energy and Materials Research, Beijing Institute of Technology, Beijing 100081, China
[b] State Key Laboratory of Advanced Chemical Power Sources, Guizhou Meiling Power Sources Co., Ltd., Zunyi 563003, China
[c] Yinlong Energy Co., Ltd., Zhuhai 519000, China

ARTICLE INFO

Article history:
Received 14 August 2020
Received in revised form 1 September 2020
Accepted 8 September 2020
Available online 9 September 2020

Keywords:
Nb_2O_5@rGO nanocomposite
Microemulsion
Anode material
Sodium-ion battery

ABSTRACT

The development of novel anode materials, with superior rate capability, is of utmost significance for the successful realization of sodium-ion batteries (SIBs). Herein, we present a nanocomposite of Nb_2O_5 and reduced graphene oxide (rGO) by using hydrothermal-assisted microemulsion route. The water-in-oil microemulsion formed nanoreactors, which restrained the particle size of Nb_2O_5 and shortened the diffusion length of ions. Moreover, the rGO network prevented agglomeration of Nb_2O_5 nanoparticles and improved electronic conductivity. Consequently, Nb_2O_5@rGO nanocomposite is employed as anode material in SIBs, delivering a capacity of 195 mAh/g after 200 charge/discharge cycles at 0.2 A/g. Moreover, owing to conductive rGO network, the Nb_2O_5@rGO electrode rendered a specific capacity of 76 mAh/g at high current density of 10 A/g and maintained 98 mAh/g after 1000 charge/discharge cycles at 2 A/g. The Nb_2O_5@rGO electrode material prepared by microemulsion method shows promising possibilities for application of SIBs.

Recently, the demand for energy storage systems has surged with the development of renewable energy technology and electric vehicles. However, the uneven distribution of lithium (Li) hinder the large-scale utilization of Li-ion batteries (LIBs) [1]. Therefore, alternative energy storage technologies are being developed to fulfill future energy requirements. Sodium-ion batteries (SIBs) are promising substitutes for LIBs, owing to abundant sodium (Na) resources [2]. However, the ionic size of Na is 55% larger than Li-ions [3], leading to inferior charge storage and cyclic stability of SIBs. Thus, alternative electrode materials, with high capacity, are being pursued for SIBs [4,5].

Orthorhombic niobium pentoxide (T-Nb_2O_5) has attracted much research attention owing to its layered structure. One should note that the (001) interplanar spacing of T-Nb_2O_5 is 3.9 Å [6], which is favorable for the intercalation of Na-ions (1.06 Å). T-Nb_2O_5 has exhibited superior pseudocapacitive performance in supercapacitors, ensuring excellent energy storage capacity [7–9]. Furthermore, Lubimtsev *et al.* have employed density functional theory (DFT) to interpret the pseudocapacitive response of Nb_2O_5, they found ions adsorb with local charge transfer and low energy barrier, together contribute to the high performance [10]. Similarly, Liao *et al.* have studied various crystal structures of Nb_2O_5 and demonstrated the superior electrochemical performance of orthorhombic phase [11]. She *et al.* have fabricated T-Nb_2O_5 nanoparticles/N-doped graphene electrode (T-Nb_2O_5/NG), rendering a capacity of 83 mAh/g at 1 A/g in SIBs [12]. However, the poor electronic conductivity of Nb_2O_5 (3×10^{-6} S/cm) leads to inferior rate performance and hinders practical applications [13]. Furthermore, the formation of orthorhombic phase requires a high calcination temperature (> 600 °C), which leads to aggregation of nanoparticles.

The abovementioned issues can be solved by structural improvements and surface coatings. For instance, the formation of nanostructure can shorten the spread distance of ions/electrons, whereas carbonaceous coatings can improve electronic conductivity [14–16]. Among various carbonaceous materials, graphene renders unique advantages, such as superior electrical conductivity and high flexibility, owing to its single layer carbon atom structure. Therefore, graphene is widely used in electrode materials [17,18]. In general, the graphene-based nanocomposites are prepared by a one-step hydrothermal process, which may cause partial aggregation of nanoparticles. On the other hand, microemulsion can

* Corresponding author.
E-mail address: sunwang@bit.edu.cn (W. Sun).

https://doi.org/10.1016/j.cclet.2020.09.006
1001-8417/

provide a micro-heterogeneous medium for the generation of nanoparticles [19]. The "nanoreactors" can restrain the particle size. For instance, Mo *et al.* have prepared TiO_2 quantum dots/graphene nanosheets (TiO_2-QDs/GNs) for LIBs with excellent rate performance [20]. Thus, it is still a challenge to explore an easy method of preparing well-dispersed Nb_2O_5 composites for SIBs.

In this work, we prepared composites of T-Nb_2O_5 and reduced graphene oxide (rGO) by a hydrothermal-assisted microemulsion route, which resulted in uniformly dispersed Nb_2O_5 nanoparticles (Nb_2O_5 NPs) on rGO surface. Nb_2O_5 nanoparticles provided additional active sites for Na^+ adsorption, whereas the conductive rGO network facilitated the transfer of electrons and prevented the agglomeration of Nb_2O_5 NPs. When used as an anode in SIBs, Nb_2O_5@rGO nanocomposite delivered a capacity of 76 mAh/g at an extremely high current density of 10 A/g. The Na^+ storage kinetics are explored by using *ex-situ* structural and surface chemistry analysis. The current work demonstrates a viable route to realize the successful utilization of Nb_2O_5-based anode in SIBs.

Fig. 1 illustrates the synthesis route of the Nb_2O_5@rGO. HCl and GO aqueous dispersion were added in a microemulsion of *n*-pentanol, *n*-hexane and CTAB. Then niobium(V) ethoxide was injected into the microemulsion under vigorous agitating. The as-prepared Nb_2O_5 nanoparticles are well synthesized in water-pool nanoreactors wrapped by surfactants. Herein, HCl aqueous solution was used as an acidic catalyst to control the reaction rate [21]. Meanwhile, the nanoparticles were uniformly anchored on the surface of GO owing to electrostatic attraction under acidic conditions. Furthermore, GO was reduced to rGO during the hydrothermal process. Finally, freeze-drying was carried out before calcination to preserve the original morphology during the solvent removal.

SEM and TEM observations were carried out to analyze the microstructure of Nb_2O_5 and Nb_2O_5@rGO nanocomposite. After thermal treatment, Nb_2O_5@rGO nanocomposite exhibited a curled morphology, consisting of a wrinkled "paper"-like structure with some aggregated Nb_2O_5 nanocrystals (Fig. 2b and Fig. S1b in Supporting information). However, owing to the utilization of microemulsion during the hydrothermal reaction, most of Nb_2O_5 NPs were well-dispersed on the graphene surface. On the other hand, pure Nb_2O_5 exhibited aggregated particles due to the absence of rGO carriers (Fig. S1a in Supporting information). The HRTEM images (Figs. 2c and d) show high crystallinity of Nb_2O_5 and Nb_2O_5@rGO nanocomposite, where the interplanar spacing of 0.39 nm matching the (001) planes of T-Nb_2O_5. Hence, T-Nb_2O_5 has been successfully synthesized by using the modified hydrothermal method. The statistical analysis (inset in Figs. 2a and b) shows that the diameter of Nb_2O_5@rGO nanoparticles ranges from 15 nm to 25 nm, whereas the diameter of Nb_2O_5 nanoparticles ranges from

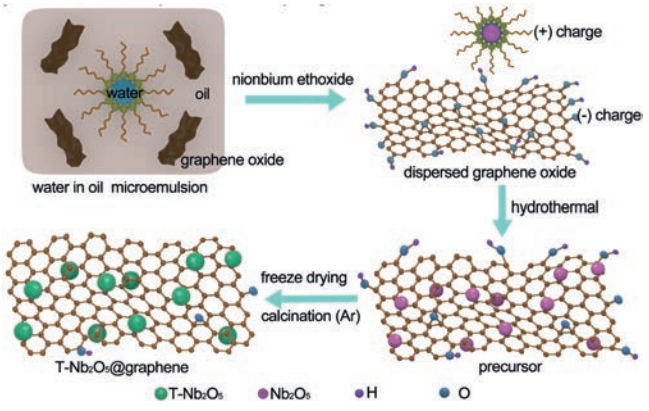

Fig. 1. Schematic illustration of Nb_2O_5@rGO nanocomposite synthesis.

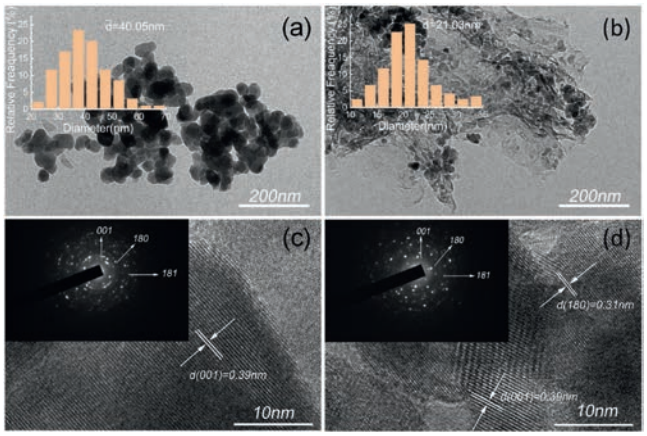

Fig. 2. TEM images of (a) Nb_2O_5 and (b) Nb_2O_5@rGO nanocomposite, where the inset shows the statistical distribution of particles' diameter. HRTEM images of (c) Nb_2O_5 and (d) Nb_2O_5@rGO nanocomposite, where the inset shows the corresponding SAED patterns.

25 nm to 55 nm. Hence, the uniform anchoring on graphene surface inhibited the further growth of Nb_2O_5 nanoparticles.

XRD patterns of as-prepared GO, Nb_2O_5 and Nb_2O_5@rGO nanocomposite are presented in Fig. 3a. Both Nb_2O_5 and Nb_2O_5@rGO exhibited similar diffraction peaks, corresponding to the orthorhombic phase of Nb_2O_5 (T-Nb_2O_5, JCPDS No. 30-0873) [22]. Furthermore, one diffraction peak in GO, located at $2\theta = 11.6°$, corresponds to (002) planes of GO, and it disappears in Nb_2O_5@rGO, indicating the successful reduction of GO into rGO. We have not observed any diffraction peak, corresponding to graphene layers at $2\theta = 26°$. Hence, the calcination process destroyed the long-range order of graphene. Raman spectra of graphene oxide (GO) and Nb_2O_5@rGO are presented in Fig. S2 (Supporting information), where two broad peaks, located at 1590 and 1350 cm^{-1}, correspond to the G- and D-bands of carbon [23]. The decrease in I_D/I_G from 1.11 to 0.98 demonstrates the successful reduction of GO. Additionally, according to TGA, the weight percentage of graphene in Nb_2O_5@rGO was found to be ~21 wt% (Fig. S3 in Supporting information).

Furthermore, Brunauer-Emmett-Teller (BET) was carried out to quantitatively examine the specific surface area of Nb_2O5@rGO nanocomposite (Fig. 3b). Nb_2O_5@rGO nanocomposite exhibited a

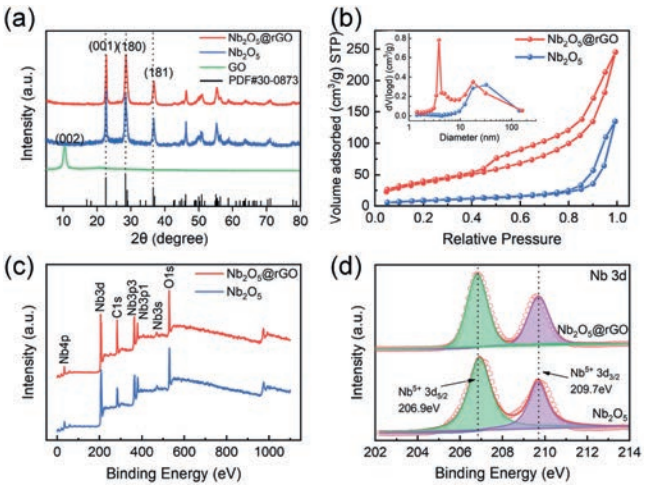

Fig. 3. (a) XRD patterns of Nb_2O_5 and Nb_2O_5@rGO nanocomposite. (b) N_2 sorption isotherms of Nb_2O_5 and Nb_2O_5@rGO (inset: pore size distribution). (c) The wide-range XPS spectra and (d) high-resolution Nb 3d XPS spectra of Nb_2O_5 and Nb_2O_5@rGO nanocomposite.

typical IV-type isotherm, revealing the presence of mesoporous. The BET specific surface area of Nb_2O_5@rGO sample is calculated as 135.7 m^2/g, whereas the mesopores are centered at 11.7 nm (Table S1). The Nb_2O_5 NPs also exhibited an IV-type isotherm, but with a lower specific surface area of 46.3 m^2/g and a larger pore size of 25.8 nm. We suggest that these pores originated from the channels between particles, which can facilitate ionic transport. Furthermore, we have carried out XPS to analyze the chemical composition of Nb_2O_5 and Nb_2O_5@rGO nanocomposite. Both Nb_2O_5 and Nb_2O_5@rGO nanocomposite contain Nb, O and C elements (Fig. 3c). The Nb 3d spectra of Nb_2O_5 can be divided into two main peaks at 206.9 and 209.7 eV, which can be assigned to the spin-orbit doublet of Nb $3d_{5/2}$ and Nb $3d_{3/2}$ (Fig. 3d) [12,24]. Moreover, high-resolution O 1s spectra can be divided into two peaks, *i.e.*, O—Nb peak (530.3 eV) and C—O peak (532.9 eV) as shown in Fig. S4a (Supporting information) [24]. XPS confirmed the successful synthesis of Nb_2O_5. Moreover, high-resolution C 1s spectra can be divided into three characteristic peaks, located at 284.7 eV, 285.8 eV and 289.2 eV (Fig. S4b in Supporting information), corresponding to C—C, C—O and C=O peak, respectively [24]. These proved there are residual oxygen-containing functional groups in rGO.

The cycle performance of Nb_2O_5 and Nb_2O_5@rGO was investigated by assembling CR2025-type coin cells. Fig. S5 (Supporting information) presents the CV curves of as-prepared Nb_2O_5@rGO electrodes. In the 1st discharge process, the broad cathodic peak corresponds to the formation of solid electrolyte interphase (SEI), which disappears in subsequent cycles. It should be mentioned that the peak at ~2.2 V also vanished after the 1st cycle, which derive from the irreversible reaction between Na^+ and oxygen-containing functional groups of rGO surface [25]. The overlapping CV curves of which electrode indicate excellent reversibility of (de)sodiation process. Furthermore, the significant redox peaks have not been observed in subsequent cycles, which indicates that the existence of pseudocapacitance. Moreover, the galvanostatic charge-discharge profiles well matches with the CV shapes (Fig. S6 in Supporting information).

Fig. 4a presents the specific capacity of Nb_2O_5 and Nb_2O_5@rGO electrodes at 0.2 A/g (1 C). One should note that the Nb_2O_5@rGO electrode exhibited a lower initial coulombic efficiency (43.5%) than Nb_2O_5 (53.7%), which can be ascribed to the larger specific surface area of Nb_2O_5@rGO. Besides, irreversible reactions occurred between Na^+ and oxygen-containing functional groups of rGO surface. However, the Nb_2O_5@rGO electrode maintained a reversible capacity of 195 mAh/g after 200 charge/discharge cycles, corresponding to a capacity retention of 92.3% based on the 20th cycle capacity. On the other hand, the Nb_2O_5 electrode maintained a specific capacity of 119 mAh/g after 200 charge/discharge cycles, which corresponds to a capacity retention of 72.5%. rGO's contribution to overall capacity of the electrode is minimal (Fig. S7 in Supporting information). Moreover, the cyclic stability of Nb_2O_5 and Nb_2O_5@rGO electrodes was evaluated at a higher current density of 2 A/g (Fig. 4c). The Nb_2O_5@rGO electrode rendered a reversible capacity of 98 mAh/g, after 1000 cycles, which is much higher than that of Nb_2O_5 electrode. Hence, the presence of graphene improved the utilization of electrochemically active sites. Fig. 4b shows the rate cycling tests of Nb_2O_5 and Nb_2O_5@rGO electrodes, measured at different current densities. Compared with pure Nb_2O_5 electrode, Nb_2O_5@rGO electrode exhibited superior rate performance and delivered a reversible specific capacity of 255, 231, 197, 173, 137, 122, 99 and 76 mAh/g at 0.04, 0.1, 0.2, 0.5, 1, 2, 4 and 10 A/g, respectively. However, the pure Nb_2O_5 electrode rendered poor rate capability at high current density due to its poor conductivity. The enhanced rate capability can be attributed to the presence of rGO and the formation of porous channels, enhancing the transfer of electrons and reducing the diffusion distance of Na^+.

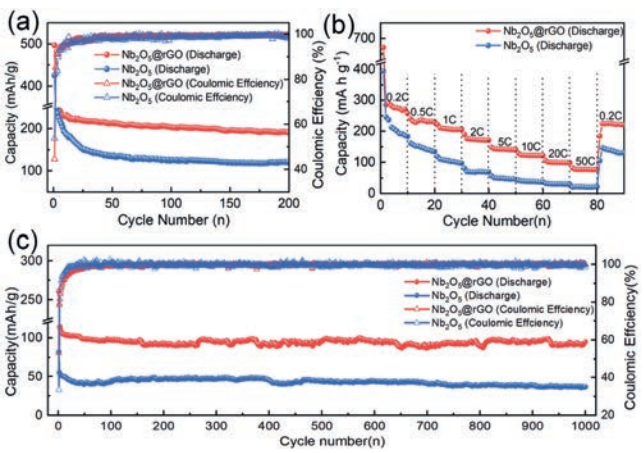

Fig. 4. Electrochemical performance of Nb_2O_5@rGO/Na cells: cyclic stability of Nb_2O_5 and Nb_2O_5@rGO at (a) 1 C (0.2 A/g) and (c) 10 C (2 A/g). (b) Rate capacities of Nb_2O_5 and Nb_2O_5@rGO electrodes at different C rates.

The electrochemical impedance spectroscopy (EIS) of as-prepared Nb_2O_5 and Nb_2O_5@rGO electrodes before cycling are measured, as exhibited in Fig. S8a (Supporting information). It is clear that the Nb_2O_5@rGO nanocomposite exhibited a much lower charge-transfer resistance (R_{ct} = 416.7 Ω) than the Nb_2O_5 nanoparticles (R_{ct} = 707.9 Ω). This can also be confirmed *via* a cross-linked rGO network, which favors rapid Na^+ transport. The diffusion coefficient of Na^+ (D_{Na}) can be evaluated from the low-frequency region of EIS by using the given relationship [26]:

$$D_{Na} = R^2T^2/2A^2n^4F^4C^2\sigma^2 \quad (1)$$

where R refers to the gas constant, T represents the absolute temperature, A corresponds to the area of the electrode, n denotes the charge number, F represents the Faraday constant, C refers to the concentration of Na-ions and σ denotes the Warburg factor (Z'). The Z' can be given as:

$$Z' = R + \sigma\omega^{-1/2} \quad (2)$$

Moreover, σ can be obtained from the graph of $Z' \sim \omega^{-1/2}$ (Fig. S8b in Supporting information). Based on Eq. (1), it can be concluded that the D_{Na} of Nb_2O_5@rGO electrode is 2.6 times higher than the Nb_2O_5 electrode. This can be ascribed to the larger contact area and shorter diffusion length of Na^+. Furthermore, we have investigated the electrochemical impedance spectroscopy of Nb_2O_5@rGO electrode after cycles. From Fig. S9 (Supporting information), it can be found that the Nb_2O_5@rGO electrode exhibited a R_{ct} value of 257.0 Ω after the 3rd cycle, which is much smaller than the R_{ct} value of as-prepared Nb_2O_5@rGO electrode. Moreover, the R_{ct} value decreased to 124.4 Ω after 10 charge/discharge cycles, which remained constant over subsequent cycles (Table S2 in Supporting information).

To further illustrate Na^+ (de)intercalation reaction in Nb_2O_5@rGO, *ex-situ* XRD and XPS analysis were carried out at different discharge/charge states during the initial cycle (Fig. 5). The diffraction peaks of T-Nb_2O_5 gradually weakened during discharge from 2.5 V to 0.01 V (*vs.* Na^+/Na) and disappeared below 0.5 V. Interestingly, the peaks did not reappear after charging (Na^+ extraction), which indicates that Na^+ intercalation led to the formation of an amorphous-like phase [27]. *Ex-situ* XPS spectra were collected at various discharge/charge states to study the oxidation state of Nb during Na^+ insertion/extraction (Fig. 5c). After discharged to 0.01 V, the peaks at 206.9 eV and 209.7 eV sharply decreased and shifted to the lower binding energy of 206.3 eV and

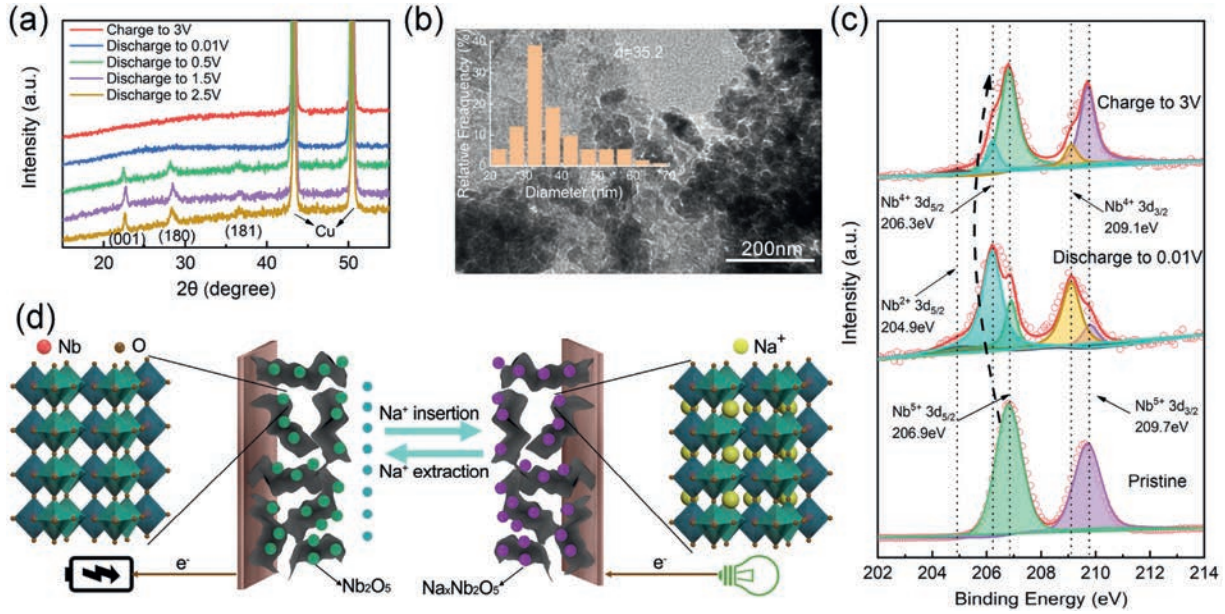

Fig. 5. *Ex-situ* analysis: (a) XRD patterns of Nb_2O_5@rGO electrodes, obtained at various discharge/charge states. (b) TEM images of Nb_2O_5@rGO nanoparticles after 100 cycles at 0.2 A/g, where the inset shows statistical analysis of the particles' diameter. (c) XPS spectra at fully discharged and fully charged states. (d) The possible charge storage mechanism of Nb_2O_5@rGO electrode.

209.1 eV, implying that the valence state of Nb atom changed from +5 to +4. Moreover, a new peak emerged at 204.9 eV, which can be ascribed to the presence of Nb^{2+}, contributing to the irreversible capacity during the initial cycle. When charging to 3.0 V, the major peaks recovered their original positions. One should note that the Nb^{2+} peak did not completely disappear after charging to 3.0 V, which implies that the formation of Nb^{2+} is an irreversible process [28]. The TEM image of Nb_2O_5@rGO after 100 cycles, measured at 0.2 A/g, further confirms that the morphology of nanoparticles is reserved during cycling (Fig. 5b). Hence, the presence of rGO network stabilized the Nb_2O_5 nanoparticles. The HRTEM image of electrochemically cycled Nb_2O_5@rGO electrode confirms the occurrence of sodiation-induced irreversible amorphization process (Fig. S10 in Supporting information). Combined with the XPS spectra and previous researches, the partially crystalline area can be ascribed to NbO [27,29]. Due to the good conductivity of NbO [30], the R_{ct} of Nb_2O_5@rGO electrode decreased after cycles, which is consistent with the EIS results (Table S2). These irreversible side reactions lead to low coulomb efficiency in the initial cycles.

Herein, we propose Na^+ (de)intercalation mechanism in Nb_2O_5@rGO electrode based on these results and published data [27], as schematically illustrated in Fig. 5d. In the first discharge, Nb_2O_5 partially transforms into NbO by conversion reactions (< 0.5 V *vs.* Na). In this process, Na ions are stored in the amorphous $Na_xNb_2O_5$ phase combined with the capacitive reactions. The formation of NbO is an irreversible process. The conductive rGO networks improve the conductivity and enlarge the contact area of electrolyte, so Nb_2O_5@rGO electrode shows superior sodium storage performances. Additionally, Table S3 (Supporting information) shows the comparisons of some Nb_2O_5-based anode materials, which are excerpted from the typical researches of SIBs in recent years. Our research work shows excellent rate performance and long lifespan.

It has been reported that T-Nb_2O_5 exhibits pseudocapacitive behavior [31]. To further explore the superior rate capability of Nb_2O_5@rGO electrode, we have studied the Na^+ storage kinetics by measuring CV curves at various scan rates (Fig. 6a). The CV data follow the power law:

$$i = av^b \tag{3}$$

$$log\ i\ =\ b\ log\ v\ +\ log\ a \tag{4}$$

where a and b are alterable constants, i refers to the current (A), and v represents the sweep rate (mV/s). As the b approaches to 0.5, the kinetic process is dominated by diffusion; as the b approaches to 1, the kinetic process is dominated by capacitive behavior [32]. Fig. 6b presents the specific peak current of Nb_2O_5@rGO at

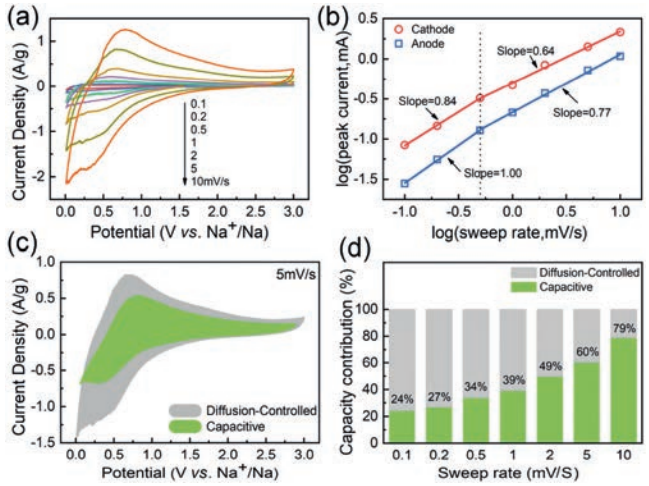

Fig. 6. (a) CV curves of Nb_2O_5@rGO electrode at different scan rates, ranging from 0.1 mV/s to 10 mV/s. (b) The linear relationship between the peak current and scan rate. (c) CV curve of Nb_2O_5@rGO electrode at 5 mV/s with separation of capacitive and diffusion currents. (d) Contribution ratio of capacitive capacity at various conditions.

different scan rates. At the scan rates of 0.1–0.5 mV/s, the *b* value of cathodic and anodic processes is found to be 0.84 and 1, respectively, indicating the current mainly originate from surface capacitive reaction. Once the scan rate exceeded 1 mV/s, the *b* values of cathodic and anodic progress reduce to 0.64 and 0.77, which suggests the kinetic process combined surface capacitive reactions with diffusion-controlled insertion reactions. The limitation at high sweep rate is caused by a diffusion limitation or an increase in ohmic impedance. The capacitive contribution of Nb_2O_5@rGO electrode, at different scan rates, can be calculated by plotting $i/v^{1/2}$ vs. $v^{1/2}$ (Figs. 6c and d). The capacitive ratio of charge storage increased from 24% to 79% with increasing scan rate from 0.1 mV/s to 10 mV/s. This demonstrates that the superior rate capability of Nb_2O_5@rGO may derive from pseudocapacitive charge storage behavior.

In conclusion, we have described Nb_2O_5@rGO nanocomposite anode for Na-ion batteries by using a water-in-oil hydrothermal-assisted microemulsion route. The nucleation and growth of Nb_2O_5 particles are assisted by the formation of nanoreactors in W/O microemulsions. The Nb_2O_5@rGO nanocomposite shows superior sodium storage. We have achieved a reversible capacity of 195 mAh/g at 0.2 A/g, and 98 mAh/g at 2 A/g, after 200 and 1000 charge/discharge cycles, respectively. The excellent properties can be attributed to the synergistic influence of Nb_2O_5 nanoparticles and two-dimensional layered structure of rGO. One should note that the nanoparticles shortened the diffusion length of ions/electrons and the graphene network prevented the agglomeration of nanoparticles. Moreover, the electrically conductive graphene network is conducive to superior rate performance. We further revealed that the Nb_2O_5@rGO stores Na^+ through partially reversible $Nb^{+4/+5}$ redox reactions, combined with surface capacitive reactions, and the pseudocapacitive charge storage behavior helps to improve the rate performance. These methods and electrode materials show promising possibilities for application of SIBs, and it is helpful to ameliorate the electrical conductivity of other similar particles.

Declaration of competing interest

The authors report no declarations of interest.

Acknowledgments

This work was supported by the National Natural Science Foundation of China (Nos. 21576028 and 21506012) and the Opening Project of State Key Laboratory of Advanced Chemical Power Sources (No. SKL-ACPS-C-19). The authors also thank Analysis & Testing Center, Beijing Institute of Technology.

Appendix A. Supplementary data

Supplementary material related to this article can be found, in the online version, at doi:https://doi.org/10.1016/j.cclet.2020.09.006.

References

[1] D. Larcher, J.M. Tarascon, Nat. Chem. 7 (2015) 19–29.
[2] Z. Jian, W. Han, X. Lu, et al., Adv. Energy Mater. 3 (2013) 156–160.
[3] M.D. Slater, D. Kim, E. Lee, et al., Adv. Funct. Mater. 23 (2013) 947–958.
[4] D. Pech, M. Brunet, H. Durou, et al., Nat. Nanotechnol. 5 (2010) 651–654.
[5] J. Liu, L. Zhang, H.B. Wu, et al., Energy Environ. Sci. 7 (2014) 3709–3719.
[6] X.L. Wang, G. Li, Z. Chen, et al., Adv. Energy Mater. 1 (2011) 1089–1093.
[7] S. Shen, S. Deng, Y. Zhong, et al., Chin. Chem. Lett. 28 (2017) 2219–2222.
[8] T. Liu, Y.F. Guo, Y.M. Yan, et al., Carbon 106 (2016) 84–92.
[9] Y. Wan, Z. Yang, G. Xiong, et al., J. Mater. Chem. A 3 (2015) 15386–15393.
[10] A.A. Lubimtsev, P.R.C. Kent, B.G. Sumpter, et al., J. Mater. Chem. A 1 (2013) 14951–14956.
[11] J. Liao, R. Tan, Z. Kuang, et al., Chin. Chem. Lett. 29 (2018) 1785–1790.
[12] L. She, Z. Iran, L. Kang, et al., ACS Omega 3 (2018) 15943–15951.
[13] J. Lin, Y. Yuan, Q. Su, et al., Electrochim. Acta 292 (2018) 63–71.
[14] J. Mei, T. Liao, Z. Sun, J. Energy Chem. 27 (2018) 117–127.
[15] Y. Chen, B. Wang, T. Hou, et al., Chin. Chem. Lett. 29 (2018) 187–190.
[16] G. Wang, Z. Wen, L. Du, et al., RSC Adv. 6 (2016) 39728–39733.
[17] H. Xu, L. Ma, Z. Jin, J. Energy Chem. 27 (2018) 146–160.
[18] B. Xu, S. Qi, M. Jin, et al., Chin. Chem. Lett. 30 (2019) 2053–2064.
[19] M.S. Lee, S.S. Park, G.D. Lee, et al., Catal. Today 101 (2005) 283–290.
[20] R. Mo, Z. Lei, K. Sun, et al., Adv. Mater. 26 (2014) 2084–2088.
[21] E. Lim, C. Jo, M.S. Kim, et al., Adv. Funct. Mater. 26 (2016) 3711–3719.
[22] L. Qin, S. Xu, Y. Liu, et al., Chin. Chem. Lett. 31 (2020) 1030–1033.
[23] W. Li, Z. Yang, M. Li, et al., Nano Lett. 16 (2016) 1546–1553.
[24] H. Yang, R. Xu, Y. Gong, et al., Nano Energy 48 (2018) 448–455.
[25] Y.X. Wang, S.L. Chou, H.K. Liu, et al., Carbon 57 (2013) 202–208.
[26] Y. Liu, L.Z. Fan, L. Jiao, J. Mater. Chem. A 5 (2017) 1698–1705.
[27] H. Kim, E. Lim, C. Jo, et al., Nano Energy 16 (2015) 62–70.
[28] N. Li, F. Zhang, Y. Tang, J. Mater. Chem. A 6 (2018) 17889–17895.
[29] Y. Wu, X. Fan, R.R. Gaddam, et al., J. Power Sources 408 (2018) 82–90.
[30] J. Li, W.W. Liu, H.M. Zhou, et al., Rare Met. 37 (2018) 118–122.
[31] V. Augustyn, E.R. White, J. Ko, et al., Mater. Horiz. 1 (2014) 219–223.
[32] J.W. Kim, V. Augustyn, B. Dunn, Adv. Energy Mater. 2 (2012) 141–148.